Millimeter-Wave and Sub-THz Phased-Array Imaging Systems Based on Electro-Optic Up-Conversion and Optical Beamforming

Dennis W. Prather , *Fellow, IEEE*, Janusz A. Murakowski , Christopher Schuetz , Shouyuan Shi , Garrett J. Schneider , Charles Harrity, Zion D. Aranda, Dominic Marinucci, Amjed Hallak, Mathew Zablocki, Matthew Gallion, Samhit Dontamsetti , Brian J. Goodman, Jesse Semmel, and Robert Lawrence

(Invited Paper)

Abstract—This article presents a class of phased-array systems that function as video-rate imagers in the millimeter-wave (mmW) and sub-THz bands. While the systems presented operate in the Ka-band (35 GHz) and W-band (77 and 86 GHz), the approach is scalable to the THz regime. Their operation is based on the upconversion of incident mmW and sub-THz signals to the optical domain using high-speed electro-optic modulators (EOMs) that are connected to each antenna element in a phased-array antenna. The output optical fiber from each EOM is relayed to a fiber bundle, or optical fiber array, from which the upconverted mmW/sub-THz signals are launched into free space. Because the upconversion preserves both the temporal and spatial coherence, through a spatial phase-control loop (SPCL), the launched sideband signals re-form the beamspace of the incident mmW or sub-THz signals, but in the optical domain. At this point, a lens performs a 2D spatial Fourier transform, to produce a real-time image of the mmW or sub-THz signals from the environment on a short-wave infrared (SWIR) camera, which renders the scene at video rates. The fundamental operating principles of these systems are presented, along with the historical progress in their development, and experimental demonstrations.

Index Terms—Beamforming, microwave photonics, optical coherent detection, phased-array antennas, radio over fiber, wireless communications.

I. Introduction

EARLY radiometric sensing/imaging dates back to WWII, where it leveraged the advent of radar technology [1], [2]. For decades, these systems consisted of single-channel radiometers due to the lack of more suitable technologies needed for real-time imaging systems. In the 1970s and 1980s their development evolved into linear and conical scanning systems [3], [4], [5]. The 1990s saw significant developments in microwave monolithic integrated circuits (MMICs) [6], [7], which led to lens-based [8], [9] mmW focal-plane-array (FPA) imaging systems [10], [11], [12], [13], [14], [15]. In the late 1990s and early 2000s novel scanning and phased-array implementations were introduced [16], [17], [18] and in the 2010s, systems based on diode detectors [19], [20], [21], [22] and cooled microbolometers were developed [23], [24], [25]. Throughout this time, applications evolved from spaceborne remote sensing to navigational aids in harsh environments, to security screening systems, and most recently to include applications of enhanced situational awareness in challenging environments [26], [27], [28], [29], [30]. All things considered, the history of radiometric imaging and related technologies is long and illustrious!

In addition to those outlined above, methods based on optical detection of mmW and sub-THz signals have also been proposed [31], including methods based on optical beamforming [32], [33]. However, the implementation of optical beamforming was limited due to the inability to achieve large-scale spatial phase coherence. This article revisits the optical beamforming approach, based on the development of a spatial phase-control-loop (SPCL) technique [34] that preserves spatial coherence of the upconverted mmW or sub-THz signals across a phased-array aperture [35], [36], [37], [38], [39]. Consequently, the incident radio signals, now in the optical domain, can be processed using a standard Fourier transform optical lens, which can process a nearly unlimited number of beams each with multiple GHz of signal bandwidth.

The optically enabled phased-array architecture underlying the systems presented in this work can be applied to a wide range of applications and frequency bands. These include image-wise detection of active microwave signals with baseband waveform recovery for communications [40], as well as microwave signal generation via downconversion between pairs of optical beams offset in frequency and spatially separated, using Fourier optics to convert the spatial separation into a beam tilt that generates a phase gradient that is preserved upon downconversion at an array
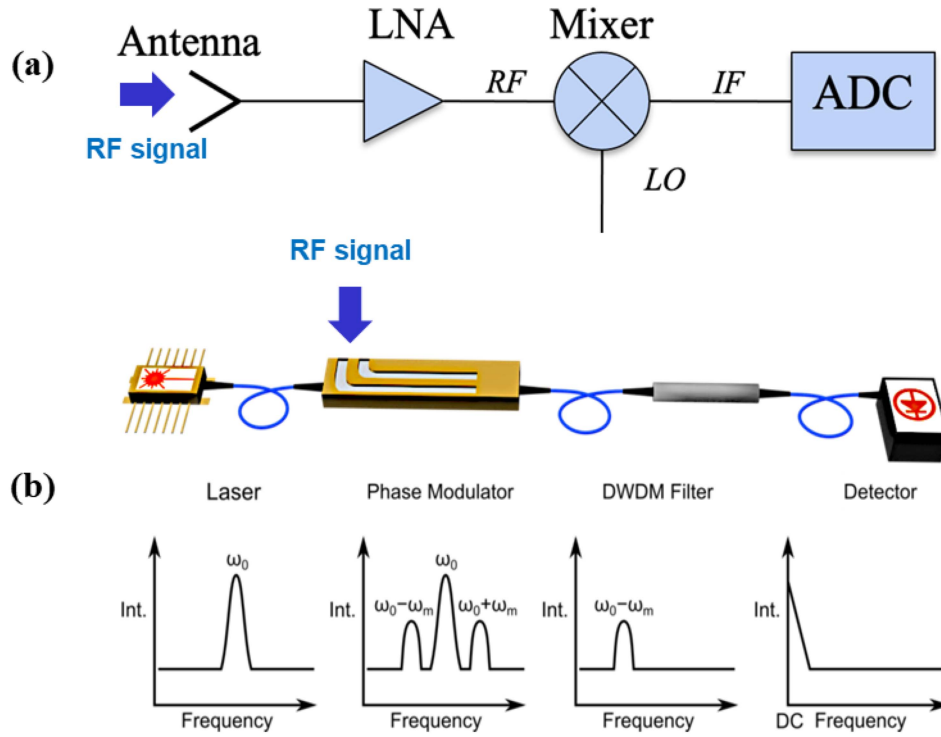
Fig. 1. (a) Conventional RF receivers downconvert the received signal using a mixer and local oscillator. (b) Optical upconversion receiver that upconverts the received RF signal onto the sideband of an optical carrier. A dense wavelength-division multiplexing (DWDM) optical filter passes one sideband and rejects the carrier and the other sideband. The passed sideband is integrated in a photodetector, yielding an output current proportional to the incident RF power.

of photodiode-fed antenna elements [40], in a manner similar to the THz beam steering approach of [41], [42]. However, it should be emphasized that the application being addressed in this article is to render mmW and sub-THz images of *passive*, i.e., thermally generated, emissions from the environment (like long-wave infrared (IR) thermal imaging but in the mmW and sub-THz region of the spectrum). For this reason, the sensitivity of these systems is quantified in terms of their noise-equivalent temperature difference (NETD).

The effective operational range of these systems is limited by the performance parameters that define the fidelity of the rendered image, such as angular resolution (denoted by $\Delta\theta$), spatial resolution (denoted by $\delta \equiv R \times \Delta\theta$, where R is the range), and NETD. The resolution is governed by diffraction, which is based on the ratio of wavelength (λ) to aperture size (D): $\Delta\theta = \lambda/D$. Thus, the primary way to improve (reduce) δ is either to decrease λ or increase D, which implies either the use of higher operational frequencies (hence mmWs or sub-THz) or a larger system aperture, or both. The sensitivity is the level at which the system can differentiate between a signal and background noise, and is thus largely based on system noise performance, which is especially challenging for *passive* imaging systems working at mmW/sub-THz frequencies, where the spectral power density of thermal (Planck black-body) emissions is $\sim 10^4$ times smaller than that at infrared frequencies for terrestrial temperatures. Because they image the radiometric environment based on variations in the brightness temperature, or thermal emissions, of objects in the scene, these systems need to be sensitive enough to render spatial variations in brightness temperature

from objects or reflections of objects from the environment, e.g., the cold sky.

As stated above, the basis for the presented approach is upconversion of mmW or sub-THz signals to the optical domain. In the systems presented herein, this is achieved using high-speed EOMs made in lithium niobate [43], [44], [45], [46]. As illustrated in Fig. 1, this approach differs from conventional radio-frequency (RF) receivers, which downconvert received signals to an intermediate frequency (IF). In this case, the upconverted signal can be represented by its electric field amplitude as follows [38]:

$$E_{\text{FSB}} \propto E_{\text{opt}} E_{\text{m}} e^{i(\omega_{\text{opt}}+\omega_{\text{m}})t+i\varphi_{\text{m}}+i\varphi_{\text{opt}}}, \tag{1}$$

where ω_{opt} and φ_{opt} are, respectively, the angular frequency and the phase of the optical carrier, while ω_{m} and φ_{m} are the angular frequency and phase of the received mmW signal. E_{FSB}, E_{opt} and E_{m} are the field amplitudes of the first optical sideband, optical carrier, and received mmW signal, respectively. Examination of (1) shows that the upconversion process yields an optical sideband signal with an amplitude proportional to both the mmW signal E_{m} and the optical carrier, E_{opt}. Also, the phase φ_{m} of the signal received at each antenna element is preserved. A main challenge, however, is the optical phase term, φ_{opt} which, in general, is random-valued due to continuously varying micro-perturbations within the optical fiber from the environment. Thus, as the upconverted signals are relayed from the antenna elements to the fiber bundle, perturbations within the optical fiber itself serve to decorrelate their phases, thereby preventing the use of an optical Fourier-transform lens to do
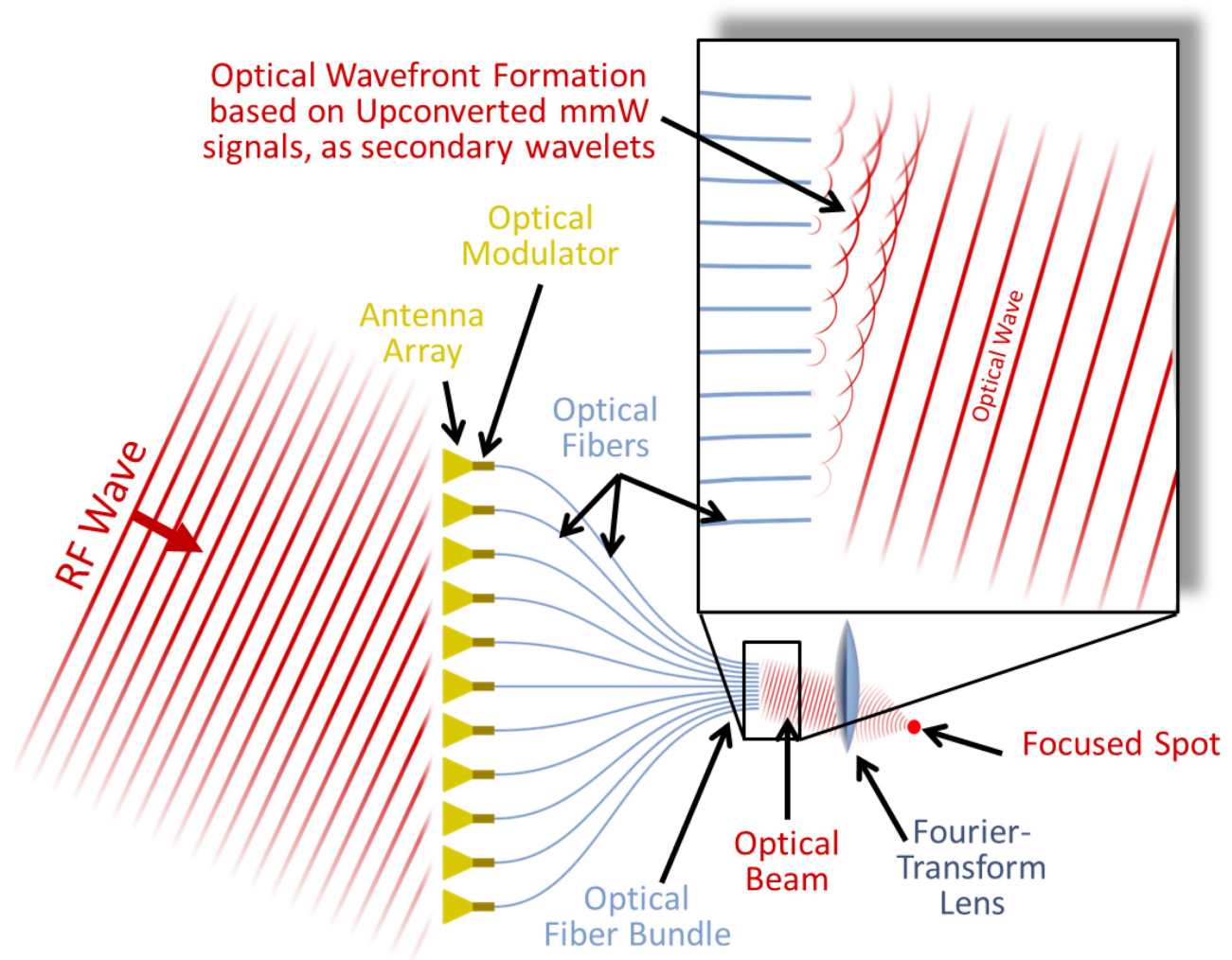
Fig. 2. Diagram illustrating the use of optical beamforming to process upconverted mmW signals to form a real-time, video-rate image of the mmW scene.

beamforming. To address this challenge, an active SPCL was developed; details of its design and function are presented in [34], while a description of the specific implementation used in the mmW imaging systems presented in this article can be found in Section IV. Therefore, the analysis presented below assumes that E_{opt} and φ_{opt} are uniform across the fiber bundle, with amplitude uniformity, E_{opt}, arising from equal splitting of a single source laser (which also inherently preserves temporal coherence), and uniformity of φ_{opt} arising from the SPCL. Note, since φ_{opt} is uniform across the array, it can be disregarded in the present context of far-field mmW imaging. However, it is worthwhile to note that the ability to control φ_{opt} afforded by the SPCL can be used to encode any desired phase profile, such as a quadratic, to enable the phased array system to perform near-field or even confocal imaging. More generally, the ability to apply any arbitrary phase profile enables point-spread-function engineering [47].

In addition to providing the ability to control the optical phases that enables imaging of the mmW scene, the optical mmW detection and beamforming approach also has the advantage of de-coupling the high-frequency electronic components in the

front end from the spatial processing and detection that follows. This means that the same frequency-agnostic optical processor can be coupled in a plug-and-play manner to a selection of front ends operating anywhere from sub-6-GHz wireless telecom bands up to the THz domain. Further, unlike conventional phased arrays, in this approach, all the beams accessible to the array (based on the aperture size and number of elements) are formed simultaneously at light speed, without the power consumption and latency of digital signal processing.

II. BASIS OF OPERATION

On a qualitative level, the operation of the imaging system can be described with the help of Fig. 2, which shows an RF wave, arriving from the left, incident onto an array antenna where each antenna element is connected directly to an EOM. The output optical fibers from each element are gathered to a common bundle, at whose termination they form an optical fiber array, where the arrangement of the fibers mimics the antenna arrangement at reduced scale. At this point, the optical signal from each fiber is launched into free space wherein the

upconverted mmW sidebands are filtered from the carrier and allowed to expand and overlap with optical signals from the other fibers. Because each optical sideband contains the amplitude and phase of the incident mmW signal, see (1), the overlaid signals recreate the mmW beamspace in the optical domain. Finally, an optical lens is used to perform the two-dimensional spatial Fourier transform [48] at the speed of light and consuming no power. (It is worth noting that, for active-signal applications such as radar and communications, this approach has a near-infinite beam-bandwidth product (BBP).)

From an imaging perspective, the mmW scene can be thought of as a distribution of thermal point sources, which are all temporally and spatially uncorrelated. As spherical waves from the point sources expand and propagate outward into the far field, they become, at the receiving aperture, a collection of uncorrelated plane waves, which is a spatial Fourier transform of each point-source distribution in the sense of Fraunhofer diffraction [48]. Effectively, the antenna array samples each plane wave and thereby captures its amplitude and phase at each antenna element location, or sample point. This amplitude and phase distribution of the mmW scene is upconverted, re-launched into free space from the fiber bundle, and ultimately inverse-Fourier transformed in the optical domain by a simple lens.

An important caveat to consider is that like all phased-array antennas that operate over a finite bandwidth, the arrays implemented in the presented passive mmW imaging systems also exhibit angle-frequency dispersion, commonly referred to as "squint." As a result, off-axis incidence plane waves having different frequencies but incident from the same direction will excite the array elements with different phase profiles, and hence they will be imaged at different locations. The phase profiles are determined by the projection of the aperture size along the direction of incidence relative to the RF wavelength, or equivalently, by the time delay between the nearest and farthest array elements multiplied by the RF frequency. In the continuous limit wherein a single point source emits over a finite bandwidth, this effect will cause its image spot to be spread out, degrading the imager's spatial resolution. The squint effect increases with both the signal bandwidth and the angle of arrival, hence the impact can be minimized by narrowing the RF bandwidth that the system receives, and by narrowing the angular range (i.e., the spatial-frequency bandwidth) that the system receives. On the other hand, increasing the RF bandwidth is desirable to improve the sensitivity, as the total power received by the system is proportional to its RF bandwidth. Likewise, increasing the spatial bandwidth (aperture size) is desirable to improve angular resolution. Therefore, the impact of squint can be understood as imposing a tradespace among the system's RF integration bandwidth, its angular field of regard (FoR), and angular resolution. Put another way, incoherent thermal sources can be considered to be superpositions of coherent (i.e., monochromatic, continuous-wave) sources with uncorrelated phases. By limiting the bandwidth of the receiver, we implicitly define a coherence time, specifically the reciprocal of the limited bandwidth. Multiplying this by the speed of light gives the coherence length. So long as the aperture size projected along the angle of incidence is smaller than this coherence length,

incoherent signals' phases remain correlated, i.e., effectively coherent, and the signals may be imaged with minimal squint degradation. Therefore, it is essential that the system be as efficient as possible in its upconversion of mmW signals, to allow narrow RF bandwidths while still achieving desired sensitivity. The systems presented in this article have demonstrated NETDs below 1 K at a video rate of 30 Hz.

The next section presents a more formal analysis of a general phased array used as a real-time imaging system, such as was described qualitatively above.

III. IMAGING SYSTEMS WITH PHASED-ARRAY ANTENNAS

This section presents the formulation of a conventional incoherent point-wise image reconstruction wherein the mmW image is reconstructed in the optical domain. As stated above, each antenna element is connected to an EOM with the output being carried in an optical fiber to a fiber bundle that terminates in an arrangement that mimics the spatial distribution of the antennas. The output of the bundle creates beams that are then allowed to interfere in free space, and the interference pattern, corresponding to the original mmW scene, is captured by a regular array of optical sensors such as a SWIR charge-coupled device (CCD) camera. The image reconstruction process can be expressed as the follows:

$$C_n = \frac{1}{\sqrt{N}} \sum_{m=0}^{M-1} B_m e^{i(\theta_{nm} + \varphi_m)} \qquad (2)$$

where B_m is the amplitude of the field at the output of the mth fiber, C_n is the amplitude of the field at the nth pixel of the CCD, φ_m is the (mmW-modulated) phase of the optical beam in the mth fiber, and θ_{nm} is the phase the optical beam picks up as it propagates in free space from m^{th} fiber to n^{th} pixel; it is assumed that there are M optical fibers, N sensing elements in the CCD array, and that the intensity of light coming out of each fiber is evenly distributed among the N sensors of the CCD. See also Fig. 3 for the parameter definitions.

For now, we assume that the scene consists of K point thermal sources that emit mmW incoherently. For simplicity, we first consider a single-tone emission. In the case of upconversion by phase modulation, the phases in the individual M channels are:

$$\varphi_m = \sum_{k=0}^{K-1} S_k \cos\left(\Omega t + \phi_{km}\right) \qquad (3)$$

where Ω is the mmW angular frequency, t is the time, and ϕ_{km} is the phase picked up by the mmW on the way to the antenna; it depends on both the scene element, index k, and on the channel, index m. S_k are the (real, time-independent) amplitudes of the mmW sources scaled by the modulation efficiency of the modulators and the distance from the mmW source to the receiving antenna (i.e., dimensionless). Identical modulation efficiency is assumed for modulators in all channels.
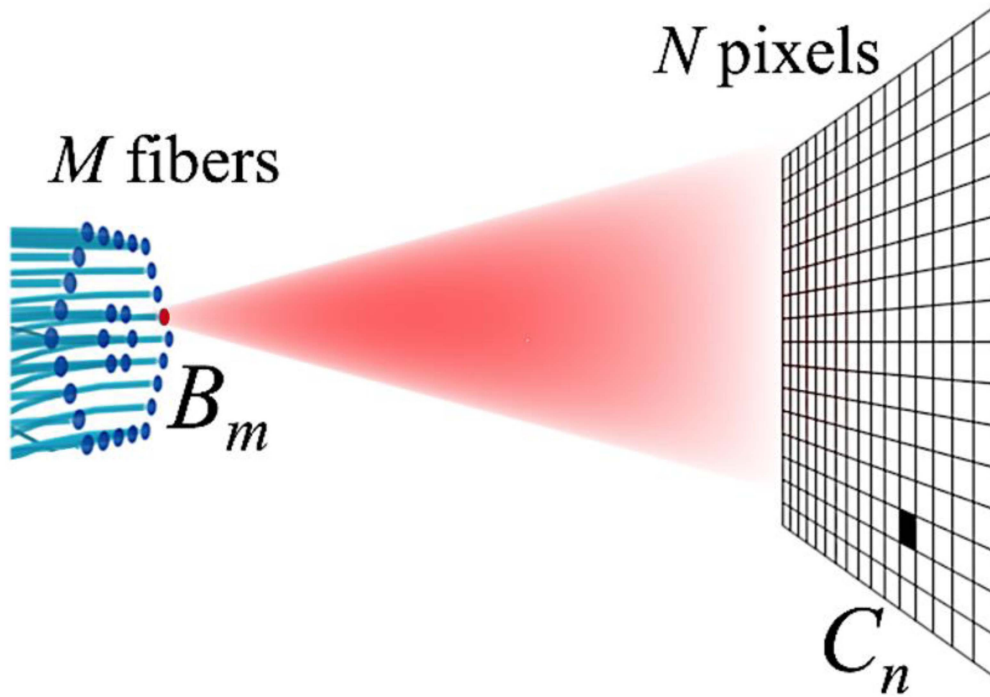
Fig. 3. Diagram representing the mathematical formulation of the optical beamforming process.

Substituting (3) into the (2) yields optical-field amplitude

$$C_n = \frac{1}{\sqrt{N}} \sum_{m=0}^{M-1} B_m \exp\left[i\left(\theta_{nm} + \sum_{k=0}^{K-1} S_k \cos\left(\Omega t + \phi_{km}\right)\right)\right]. \tag{4}$$

Element n of the photo-detector array senses the time-averaged power of light incident upon it, i.e., $P_n = \langle|C_n|^2\rangle = \langle C_n C_n^*\rangle$, where the asterisk indicates complex conjugation. In the monochromatic analysis of uncorrelated sources considered here, time averaging, indicated by angled brackets $\langle\ \rangle$, may be expressed mathematically by averaging over all possible phase offsets among the sources—see, e.g., (7) below.

In the small-signal regime, $\sum_k |S_k| \ll 1$, only the lowest-order terms in the Taylor expansion of the exp function in $|C_n|^2$ contribute significantly to the result, and therefore only those terms are retained. Of these, terms linear in S_k average to zero, as do cross-correlation terms containing $S_k S_{k'}$ for $k \neq k'$, since the sources are assumed uncorrelated. With these observations the average power P_n incident on the nth photo-detector becomes

$$P_n = \left\langle|C_n|^2\right\rangle = \langle C_n C_n^*\rangle = \frac{1}{N} \sum_{m,m'} B_m B_{m'}^* e^{i(\theta_{nm} - \theta_{nm'})}$$

$$\times \left\langle 1 - \frac{1}{2}\sum_k S_k^2 \left[\cos\left(\Omega t + \phi_{km}\right) - \cos\left(\Omega t + \phi_{km'}\right)\right]^2\right\rangle. \tag{5}$$

Linearity of the averaging operation allows rewriting the last term in (5) as

$$1 - \frac{1}{2}\sum_k S_k^2 \left\langle\left[\cos\left(\Omega t + \phi_{km}\right) - \cos\left(\Omega t + \phi_{km'}\right)\right]^2\right\rangle. \tag{6}$$

Averaging in (6) consists of integration over a uniform probability distribution of phase ϕ_k associated with k^{th} source:

$$\left\langle\left[\cos\left(\Omega t + \phi_{km}\right) - \cos\left(\Omega t + \phi_{km'}\right)\right]^2\right\rangle$$

$$= \frac{1}{2\pi}\int_0^{2\pi}\left[\cos\left(\Omega t + \phi_{km} + \phi_k\right) - \cos\left(\Omega t + \phi_{km'} + \phi_k\right)\right]^2 d\phi_k$$

$$= 1 - \cos\left(\phi_{km} - \phi_{km'}\right). \tag{7}$$

As a result, (5) becomes

$$P_n = \frac{1}{N}\sum_{m,m'} B_m B_{m'}^* e^{i(\theta_{nm} - \theta_{nm'})}$$

$$\times\left\{1 - \frac{1}{2}\sum_k S_k^2\left[1 - \cos\left(\phi_{km} - \phi_{km'}\right)\right]\right\}, \tag{8}$$

which may be split into the following two terms:

$$P_n = \left(1 - \frac{1}{2}\sum_k S_k^2\right)\frac{1}{N}\sum_{m,m'} B_m B_{m'}^* e^{i(\theta_{nm} - \theta_{nm'})}$$

$$+ \frac{1}{2N}\sum_k S_k^2\sum_{m,m'} B_m B_{m'}^* e^{i(\theta_{nm} - \theta_{nm'})}$$

$$\times \cos\left(\phi_{km} - \phi_{km'}\right). \tag{9}$$

The first term in (9) is identified as the intensity produced by the carrier wavelength of the modulated signal (no spectral filtering was applied in the calculations). It contains no information about the scene except for the total power that is shifted from the carrier frequency to the sidebands, $\frac{1}{2}\sum_k S_k^2$. The second term of (9) represents the sidebands and carries information about the scene.
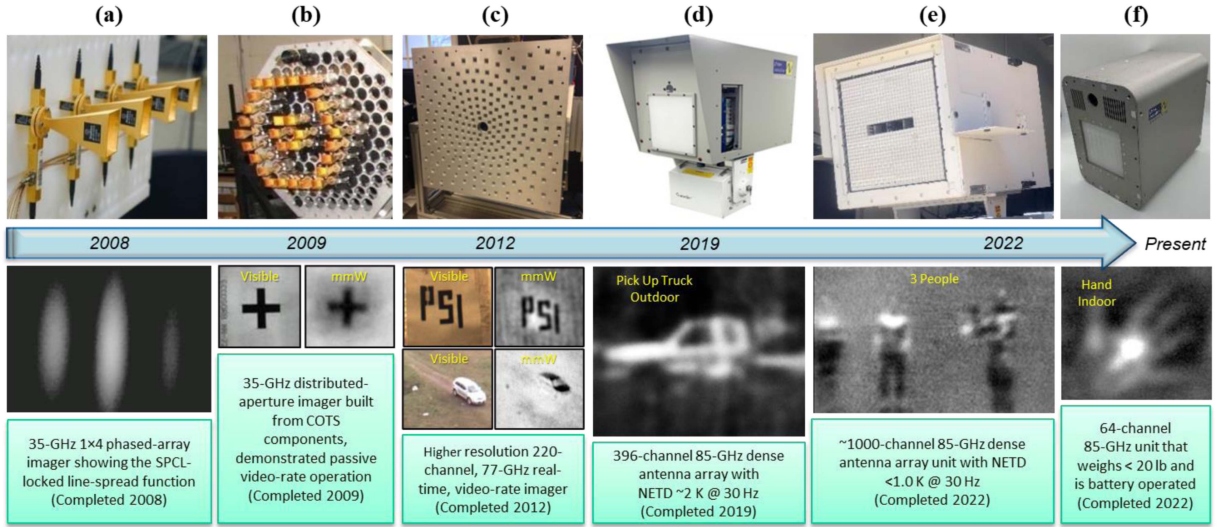
Fig. 4. Passive mmW imager development timeline starting in 2008 through 2022: (a) 1×4 array in 2008 first demonstration of the concept, (b) 32-element sparse array with first passive demonstration in 2009, (c) 220-element 5-arm spiral sparse array demonstrated in 2012 with an NETD of $\sim$5 K, (d) first full, or dense, array with $18 \times 22 = 396$ elements in 2019 with an NETD $\sim$2 K, (e) 32×32 dense array, with boresight visible and IR cameras, with an NETD $<$1.0 K, and (f) portable 8×8 dense array with an NETD $\sim$0.8 K, weight $\sim$19 lb, and able to run battery-operated for up to 4 hours with a 10-Ah battery.

It can be further manipulated to yield

$$\frac{1}{2N}\sum_k S_k^2 \sum_{m,m'} B_m B_{m'}^* e^{i(\theta_{nm}-\theta_{nm'})}\cos\left(\phi_{km}-\phi_{km'}\right)$$

$$= \frac{1}{4N}\sum_k \left|\sum_m S_k B_m e^{i(\theta_{nm}+\phi_{km})}\right|^2$$

$$+ \frac{1}{4N}\sum_k \left|\sum_m S_k B_m e^{i(\theta_{nm}-\phi_{km})}\right|^2. \qquad (10)$$

The two terms in (10) can be identified as two images reconstructed from the two sidebands of the modulated optical beam. They differ in the sign between the phases on the antenna side ϕ_{km} and on the optical side θ_{nm}. Therefore, if both sidebands were kept in the image reconstruction, two images would be present—one superimposed on the other. These images are related by center-point reflection.

For an intuitive understanding of (10), consider the second term, which corresponds to the intensities captured by the optical sensor in the presence of spectral filtering that allows only one of the sidebands to pass. Specifically, the spectrally filtered optical power captured by the nth pixel of the array is

$$P_n = \frac{1}{4N}\sum_k \left|\sum_m S_k B_m e^{i(\theta_{nm}-\phi_{km})}\right|^2, \qquad (11)$$

and can be rearranged as follows:

$$P_n = \frac{1}{4N}\sum_{m,m'} B_m B_{m'}^* e^{i(\theta_{nm}-\theta_{nm'})}\sum_k S_k^2 e^{-i(\phi_{km}-\phi_{km'})}. \qquad (12)$$

The phase angles $\theta_{nm}-\theta_{nm'}$ and $\phi_{km}-\phi_{km'}$ can be found using the positions $\mathbf{R}_m$ of the antenna elements in the antenna array, the positions $\mathbf{r}_m$ of the fibers in the fiber array, as well as the wave-vectors $\mathbf{K}_k$ and $\mathbf{k}_n$ of the incoming mmW radiation

and of the optical beam, respectively:

$$\phi_{km}-\phi_{km'} = \mathbf{K}_k \cdot (\mathbf{R}_m - \mathbf{R}_{m'}) = \mathbf{K}_k \cdot \Delta\mathbf{R}_{mm'}$$

$$\theta_{nm}-\theta_{nm'} = \mathbf{k}_n \cdot (\mathbf{r}_m - \mathbf{r}_{m'}) = \mathbf{k}_n \cdot \Delta\mathbf{r}_{mm'}. \qquad (13)$$

As a result,

$$P_n = \frac{1}{4N}\sum_{m,m'} B_m B_{m'}^* e^{i\mathbf{k}_n\cdot\Delta\mathbf{r}_{mm'}}\sum_k S_k^2 e^{-i\mathbf{K}_k\cdot\Delta\mathbf{R}_{mm'}}$$

$$= \frac{|B|^2}{4N}\sum_{m,m'}\left(\sum_k S_k^2 e^{-i\mathbf{K}_k\cdot\Delta\mathbf{R}_{mm'}}\right)e^{i\mathbf{k}_n\cdot\Delta\mathbf{r}_{mm'}} \qquad (14)$$

where it is also assumed that the optical power is evenly distributed among the M fibers, $B_m \equiv B$. Since the fiber array is a scaled version of the antenna array, $\Delta\mathbf{r}_{mm'} \propto \Delta\mathbf{R}_{mm'}$, (14) has a form of a composition of a Fourier transform with an inverse Fourier transform. Therefore, as long as the baselines $\Delta\mathbf{R}_{mm'}$ cover the Fourier domain reasonably well, it is expected that the optical image captured by the imaging array will faithfully reproduce the mmW scene. Furthermore, result (14) is consistent with the approach used in computer simulations where the scene is reconstructed point-wise, and the powers are added (incoherently) at the detectors.

The preceding discussion implicitly assumes that each of M fibers illuminates the entire array of N detectors uniformly, and does not consider the finite size of the detector array. In reality, the fibers emit a limited range of angles, with an approximately Gaussian power distribution, resulting in a gradual roll-off in optical power (and hence in NETD) toward the outer edges of the image. Further, the fiber spacing is limited in practice to be equal to or greater than the fiber diameter (typically 250 μm), which is much larger than both the optical wavelength (typically 1.55 μm) and the fiber mode diameter ($\sim$10 μm). Hence, the optical aperture that re-launches the upconverted RF field as depicted in Fig. 2 is underfilled, and hence subject to
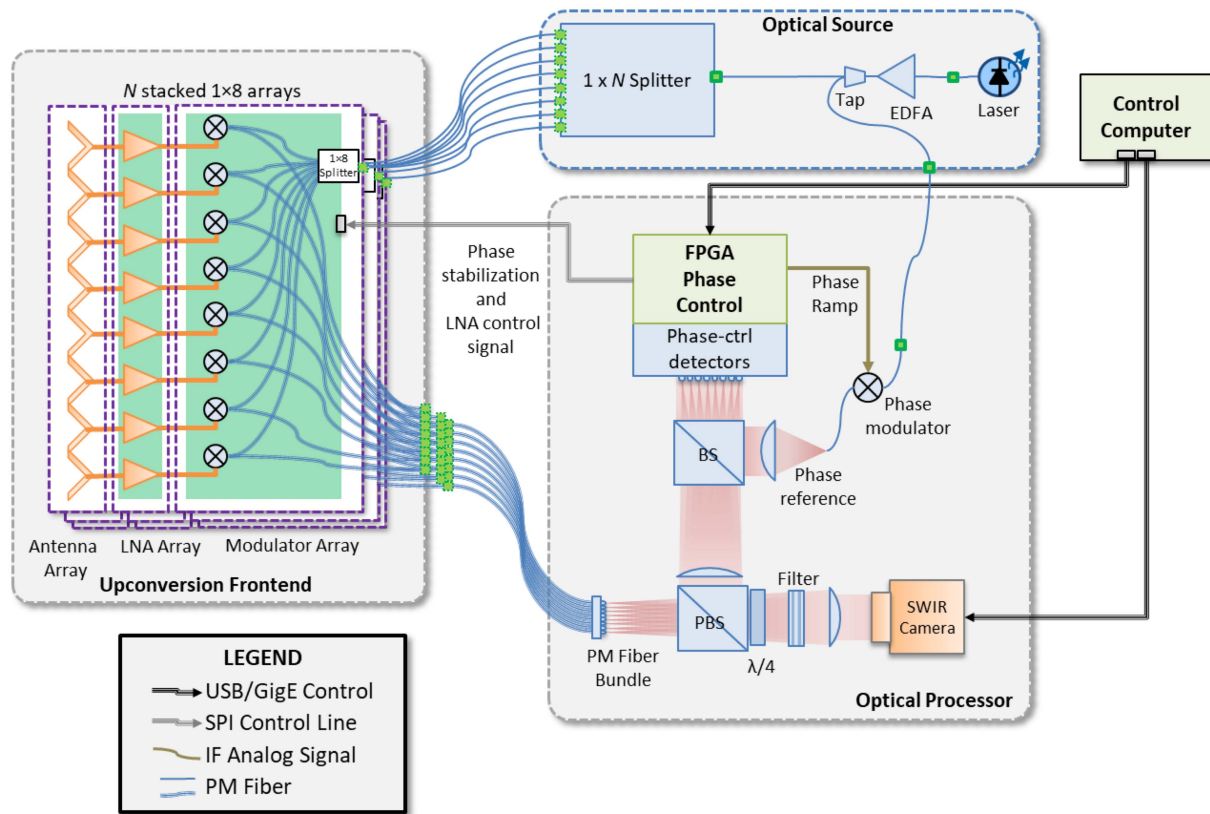
Fig. 5. Schematic block diagram of the optically upconverted phased-array architecture. (LNA: low-noise amplifier, PM: polarization maintaining, BS: beam splitter, PBS: polarizing beam splitter, SWIR: short-wave infrared, λ/4: Quarter-wave plate, EDFA: Erbium-doped fiber amplifier, FPGA: field-programmable gate array).

the formation of grating lobes. These effects are mitigated in practice by collimating the fiber outputs with microlenses, which are used to expand the optical mode size at the input focal plane of the lens to match the fiber spacing. This has the effect of limiting the angular divergence of the fiber outputs such that the area they illuminate in the output focal plane is well matched to the alias-free image size (i.e., the grating lobe spacing) on the CCD array. Additional discussion of the origin and impact of optical grating lobes in the architecture presented here, in the context of imaging active communications signals, can be found in [40].

IV. IMAGER BUILDS AND DEMONSTRATIONS

Systems based on the above formulation have been under continuous, evolving development according to the timeline in Fig. 4. Concurrently, significant effort has been focused on the requisite EOMs needed for efficient upconversion of mmW and sub-THz signals to the optical domain, with demonstrated performance up to 500 GHz [43], [44], [45], [46]. As seen in Fig. 4, various system-level architectures have been investigated. The first system to demonstrate coherent optical beamforming using a SPCL was that depicted in Fig. 4(a), which used an active source to demonstrate the line-spread function (1D) of a 1 × 4 array antenna [49]. This result was extended to a 2D

sparse array, shown in Fig. 4(b) that consisted of 30 elements in a dual-ring sparse-array antenna configuration [39], [50]. The first phased-array imaging system suitable for flight and field testing was that shown in Fig. 4(c), which was a 5-arm spiral sparse array with 220 elements distributed over a 2 × 2-ft aperture [30], [51], [52]. This system achieved an NETD of ∼5 K. Next, to improve image quality as well as the NETD, a dense-array antenna system was developed that had 396 elements in a dense 18 × 22 configuration, shown in Fig. 4(d). However, this system was found to have limitations in spatial phase locking due to the limited input/output capacity of the field-programmable gate arrays (FPGAs) that were used to implement the SPCL algorithm over the entire array. Thus, the achieved NETD was only ∼2 K. These issues were resolved in the next system to be demonstrated, a larger dense-array antenna having a 32 × 32 array configuration, see Fig. 4(e). In this system, a block of 48 elements near the center of the array was removed to provide space for a boresight-aligned IR camera and a pair of visible cameras that provide passive stereoscopic ranging. Thus, the net number of active elements was 976. This system demonstrated an NETD of <1.0 K at video rates (30 Hz). Lastly, an ultra-light system using an 8 × 8 array antenna (64 elements) was developed for flight testing on a drone, which weighs 19 lb and is battery powered for up to 4 hours with a 10-Ah battery. The measured NETD of this system is ∼0.8 K, see Fig. 4(f).
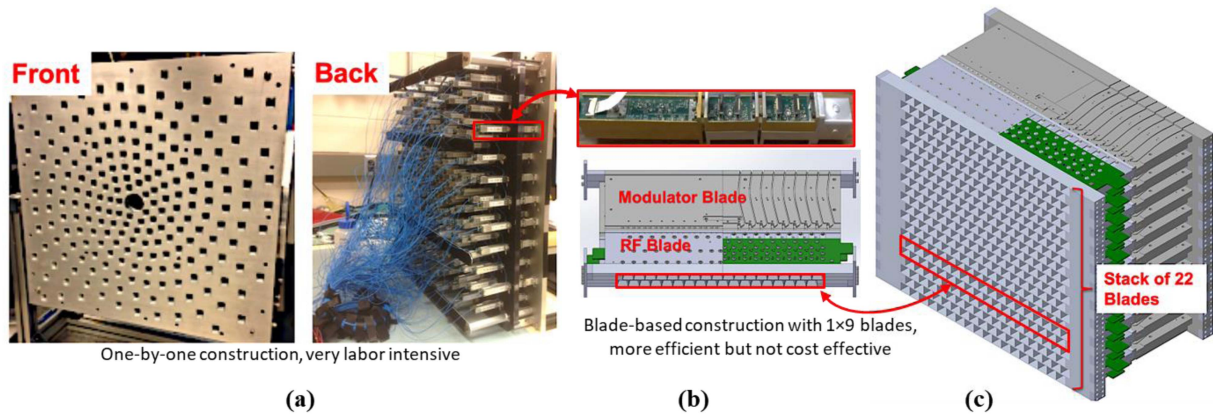
Fig. 6. Building phased-array imaging systems: (a) single RF-photonic upconversion modules, (b) transition to blade-based integration processes, and (c) stacking of the blades to realize a dense-array imager.
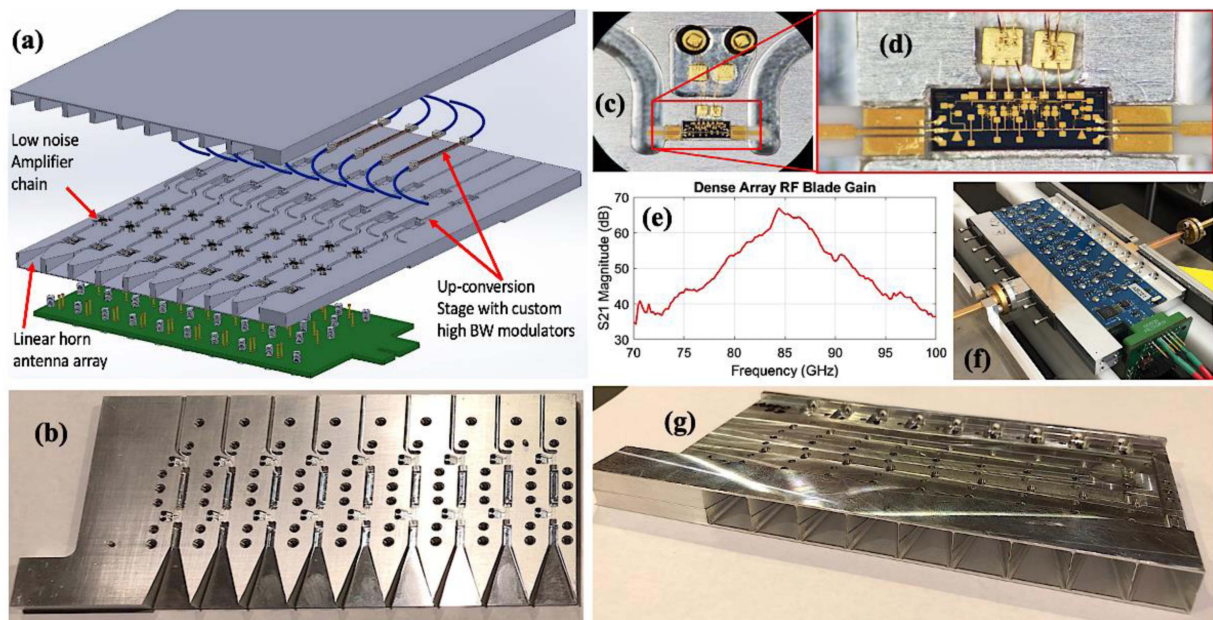

Fig. 7. RF-photonic upconversion blade integration: (a) blade-based array design and integration, (b) machined bottom half-blade, ready for integration, (c) integrated LNA in bottom housing, (d) zoom-in of LNA, (e) LNA gain measurement with peak at 85 GHz, (f) setup to test integrated blade, and (g) fully machined and integrated blade.

Through the development path just described, where necessity definitely became the mother of invention, the overall system architecture has converged to that of Fig. 5, which shows schematically the basic building blocks for a phased-array imaging system, including the use of a single laser and associated erbium-doped fiber amplifier (EDFA) to feed the entire imaging system with a single laser source, thereby ensuring temporal coherence so long as any path-length mismatches are within the coherence length of the laser. Before discussing the various aspects of this architecture, it is important to highlight the manner in which the systems' methods of construction have evolved. The first large-scale 2D array, shown in Fig. 6(a), was made by integrating each RF-photonic module individually. This process proved to be extremely time-consuming and very costly. Thus, the next generation of system was designed using a blade-based approach, where each row of the array was divided into two modules of 1 ×

9 elements. This enabled batch integration, which significantly reduced the labor associated with RF-photonic integration. However, the choice of 1 × 9 modules was short-sighted in that commercial off-the-shelf (COTS) arrayed components, connectors, and packages are most commonly available in 1 × 8 sizes, and multiples thereof. Thus, more recent versions of the phased array systems use a modulo 1 × 8 blade-based approach which proved more efficient in terms of integration and cost-effectiveness. The blade-based approach is illustrated in Fig. 6(b) and (c).

With this in mind, we return to the architecture presented in Fig. 5, where the top-left section shows the RF-photonic front end which comprises individual blades, as seen in the computer-aided-drafting (CAD) rendering of Fig. 7(a). The integrated blades are first machined with top and bottom halves, shown in Fig. 7(b). Low noise amplifiers (LNAs) are integrated into machined pockets as shown in Fig. 7(c) and (d) and subsequently
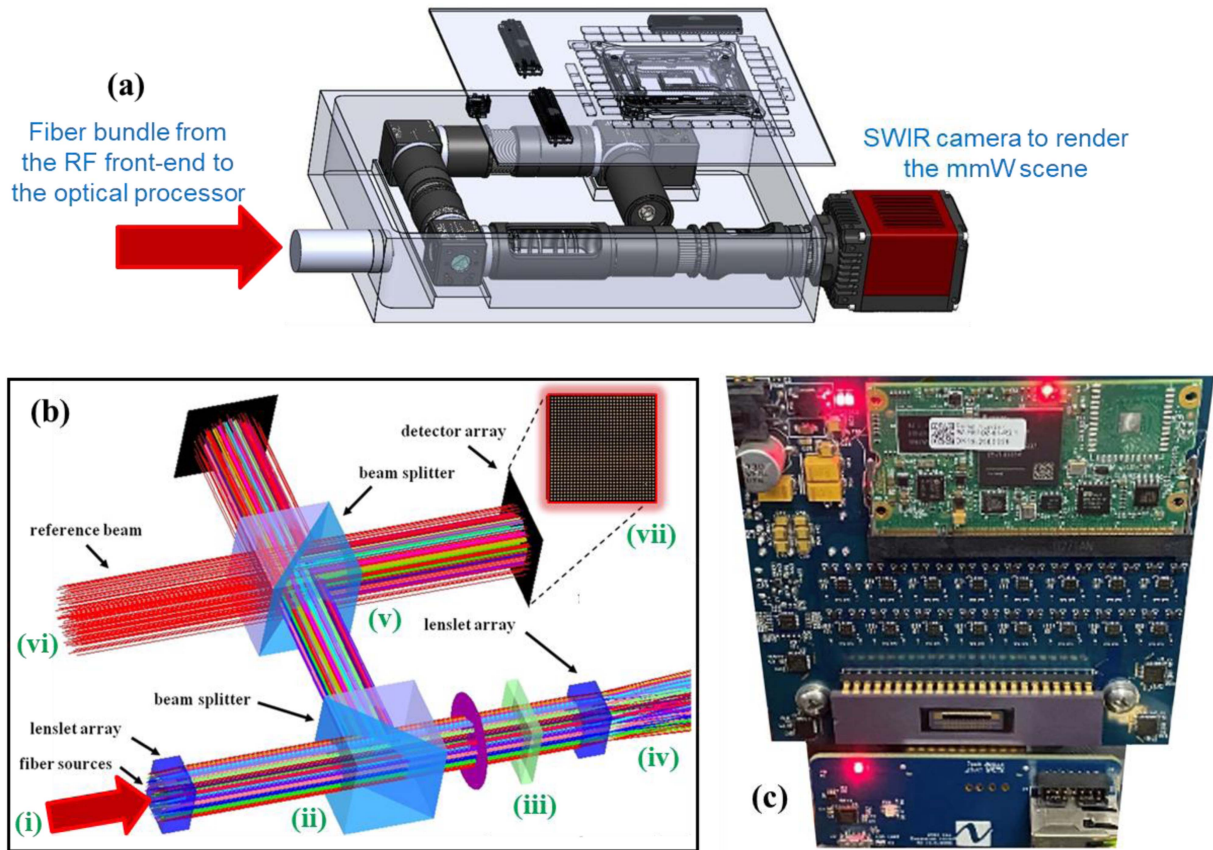
Fig. 8. Optical control system including: (a) CAD rendering of the optical processor, (b) ray-trace design and simulation of the optical processor, and (c) FPGA-based control system for the spatial phase-control loop.

tested on a vector network analyzer (VNA), as shown in Fig. 7(e) and (f). Lastly, the top halves of the blades are fastened to realize a completed front-end blade, as shown in Fig. 7(g). The LNAs used in this work consisted of two stages of Northrop Grumman ALP275 W-band LNAs with a peak gain of 68 dB at ~85 GHz. The output waveguide from the RF sub-blade couples directly to the input waveguide of the optical sub-blade, which transitions to a co-planar-waveguide (CPW) transmission line on the EOM. This is where optical upconversion occurs. The output from the optical sub-blade is an array of optical fibers that are gathered into a bundle, terminating in a fiber array, where the location of each fiber termination in the array corresponds homothetically to the location of the respective element in the antenna array. From this point, the optical signals are launched into free space within the optical processor, as shown in Fig. 8.

The optical processor, seen at the center of Fig. 5, and depicted in more detail in Fig. 8(b), replicates optically the beamspace of the incident mmW signals using a spatial Fourier transform performed by an optical lens. It also implements the SPCL, which preserves spatial coherence across the array after upconversion. To begin, the output optical fibers from the upconversion blades are gathered into a fiber array and launched into free space, as shown in Fig. 8(b)(i). After propagating through a polarizing beamsplitter (PBS) (Fig. 8(b)(ii)), the optical signals pass through a quarter-wave plate (QWP) and are incident on a thin-film-stack reflection filter (Fig. 8(b)(iii)), from which

the carriers and lower sidebands are reflected back for use in the SPCL, while the upper sidebands continue to propagate (Fig. 8(b)(iv)), ultimately reforming the mmW beamspace on a SWIR camera, seen in Fig. 8(a). After propagating back through the QWP a second time, the carriers' polarization is rotated by 90° and consequently they are reflected by the PBS toward a second beamsplitter (Fig. 8(b)(v)) that directs the now-focused carriers to an array of photodetectors (PDs) (Fig. 8(b)(vi)), where the carrier from each input fiber is focused onto a separate PD. At the same time, a reference beam, created from the same carrier laser, is introduced via the second beamsplitter as a collimated source, i.e., a spatially flat phase reference (Fig. 8(b)(vii)). This reference is phase modulated in time with a 200-kHz sawtooth waveform whose amplitude is matched to the full-wave voltage of a low-speed reference phase modulator. The reference modulation frequency is chosen to be >10 times higher than the characteristic frequencies of the (predominantly acoustic) fiber perturbations. Consequently, each focused carrier spot is overlaid with the time-modulated reference beam such that they interfere, causing the PDs to produce 200-kHz sinusoidal output signals, which deviate in phase from the reference sawtooth in direct proportion to any phase perturbations that were introduced in the optical fibers that conveyed the upconverted RF signals from the EOMs to the optical processor. These signals are digitized and processed using an FPGA control system, which also synthesizes the reference sawtooth. The FPGA computes the phase
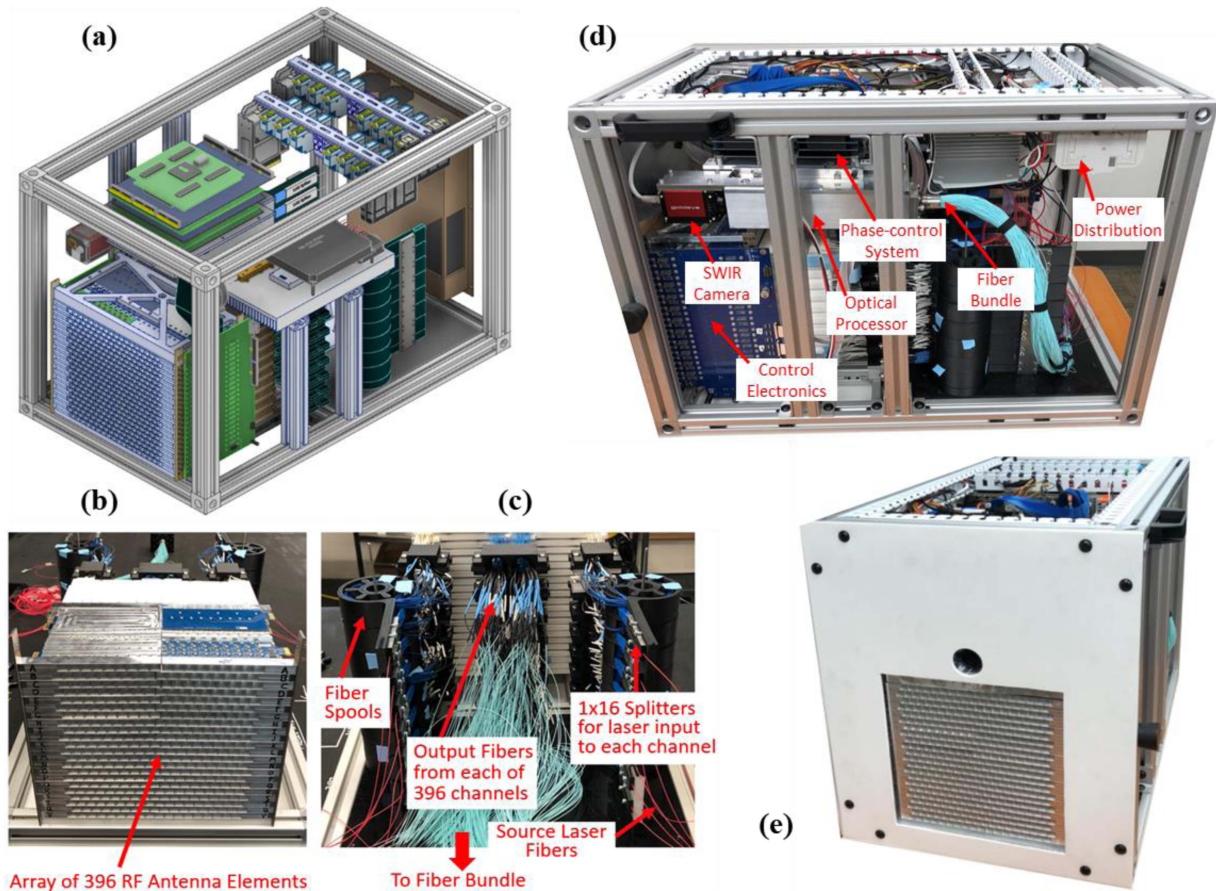
Fig. 9. Overall system design and build: (a) CAD design of a dense-array mmW video-rate imaging system, (b) array antenna during system build, (c) output optical fibers from the array, (d) side view of the imager showing the fiber bundle and optical processor, (e) final system with integrated visible camera mounted just above the array antenna.

deviation in each channel and generates a set of output voltages, one for each channel, that are fed back to bias each EOM in the array, thereby providing a real-time cancellation of the phase perturbations. The end result is the continuous preservation of spatial coherence across the array after upconversion, which allows the mmW beamspace to be imaged in the optical domain on a SWIR camera, for real-time rendering of the mmW scene.

A final, practical aspect of realizing a phased-array imaging system is building the system chassis, which consists of a power distribution system and mechanical mounts and struts that hold the various subsystem sections, as shown in Fig. 9. Fig. 9(a) shows a CAD rendering of the antenna array, RF-photonic blades, and a thermoelectric cooler mounted on the top. Fig. 9(b) and (c) are the front and rear view of the integrated and stacked upconversion modules, with the rear view showing the output optical fibers. Fig. 9(d) shows the integrated chassis with references to the key functional components of the system, including the SWIR camera, control electronics, optical processor, phase control system, fiber bundle, and power distribution.

With the system-build process described above, several real-time mmW and sub-THz imagers have been built and demonstrated. Accordingly, snap-shot images from multiple systems are shown in Fig. 10 where (a) and (b) show images of cars in a parking lot, (c) and (d) show a person kneeling in front of a truck,

(e) and (f) show a person with a concealed object under with (g) being the toy plastic pistol that was wrapped in aluminum tape. Lastly, Fig. 10(h) and (i) show a person entering a tent with someone already inside it. This image was taken in the late evening where daylight was minimal. These snap-shot images extracted from real-time videos demonstrate unique properties of mmW and sub-THz imaging systems, namely that they provide a see-through imaging capability not available in visible and IR imaging systems, and that the scene contrast, arising from the different brightness temperatures of ambient-temperature emissive objects and the cold sky, is day/night independent.

Finally, it should be noted that the emerging field of artificial intelligence and machine learning (AI/ML) is providing remarkable image-enhancement capabilities including deblurring, object identification, and subject tracking. While this topic is beyond the scope of this article, it is an exciting area of research and is likely to have significant application to mmW and sub-THz imaging, given their relatively poor image quality in comparison to visible and IR imaging systems.

V. SUMMARY

This article presented a new class of imaging phased-array systems that provide real-time, video-rate spatial rendering of
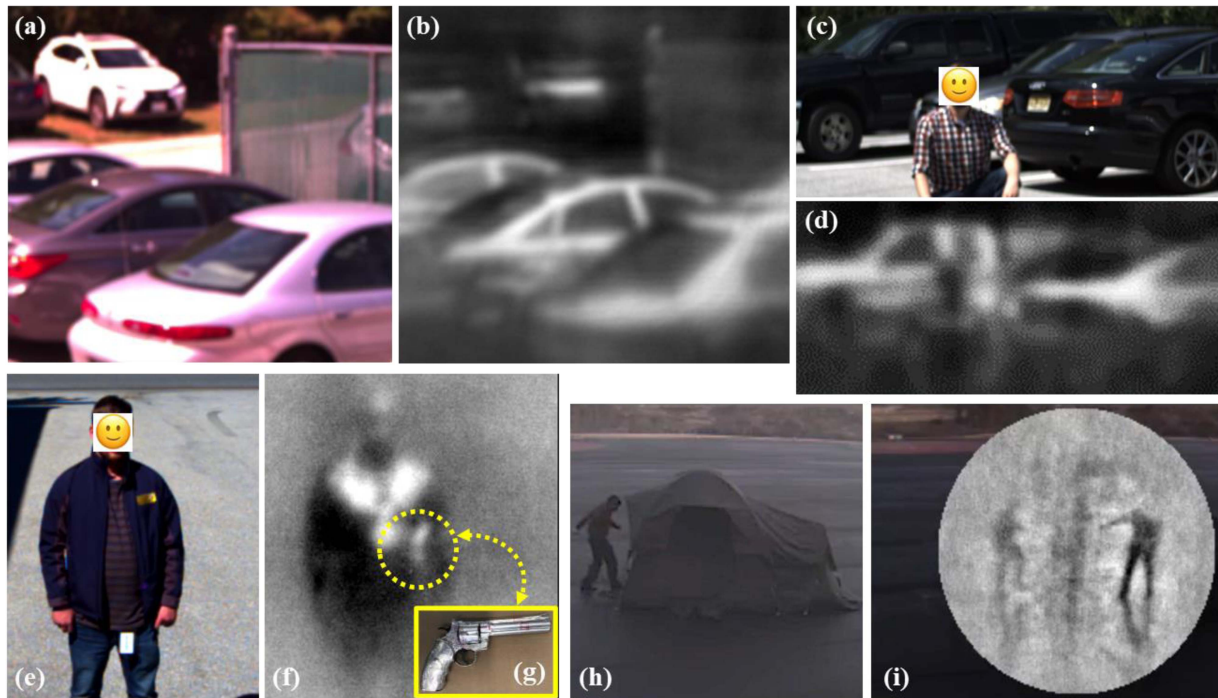
Fig. 10. Still image captures from real-time video-rate (30 Hz) mmW imaging systems: (a) visible image and (b) mmW image of parking lot; (c) visible image and (d) mmW image of a person kneeling in front of parked vehicles; (e) visible image and (f) mmW image of a person with a concealed toy pistol, where the concealed pistol in the right pocket can be seen clearly in (f); (g) photo of the toy pistol wrapped in aluminum tape; (h) visible image and (i) mmW image of a person entering a tent with another person already inside, where both individuals are shown clearly in (i).

scenes within the mmW and sub-THz regions of the electro-magnetic spectrum. Section II described the general principles of operation and performance achieved in experimental testing whereas Section III offered a rigorous mathematical analysis of image formation. Starting from first principles and using well-justified approximations, we arrived at a general expression linking the spatially incoherent mmW radiation emanating from the scene with the image produced by interfering modulation sideband at a photodetector plane. The mathematical treatment is sufficiently general and flexible to be applicable to ana-lyzing a wide class of systems relying on spatially coherent up-conversion of radio-frequency waves to optical domain for processing, such as those presented in [40].

The progression of fabricated system architectures was pre-sented in the context of improving not only system-level perfor-mance, but also the manufacturability of the systems. To this end, an efficient, modular blade-based approach was presented that is efficient for integration and cost-effective from a commercial parts consideration. Imaging demonstrations of the most recent systems were presented that showed the ability to render high-contrast outdoor images with sub-Kelvin NETD, along with concealed object detection and imaging through structures.

Finally, it is noteworthy that the optical beamforming ap-proach presented is entirely agnostic to RF frequency, and there-fore will readily scale to frequencies in the THz regime. Only the front-end RF components, i.e., the antennas and LNAs, are frequency dependent. Presently, efforts are ongoing to develop antenna and LNA technology that will enable this approach to

be used at up to 0.2 THz, for applications such as ultra-wideband atmospheric sensing [53].

REFERENCES

[1] J. C. Wiltse, "History of millimeter and submillimeter waves," *IEEE Trans. Microw. Theory Techn.*, vol. 32, no. 9, pp. 1118–1127, Sep. 1984, doi: 10.1109/TMTT.1984.1132823.

[2] P. H. Siegel, "Terahertz technology," *IEEE Trans. Microw. Theory Techn.*, vol. 50, no. 3, pp. 910–928, Mar. 2002, doi: 10.1109/22.989974.

[3] J. P. Hollinger, J. E. Kenney, and B. E. Troy, "A versatile millimeter-wave imaging system," *IEEE Trans. Microw. Theory Techn.*, vol. 24, no. 11, pp. 786–793, Nov. 1976, doi: 10.1109/TMTT.1976.1128961.

[4] W. J. Wilson, R. J. Howard, A. Ibbott, G. S. Parks, and W. B. Ricketts, "Millimeter-wave imaging sensor," *IEEE Trans. Microw. Theory Techn.*, vol. 34, no. 10, pp. 1026–1035, Oct. 1986, doi: 10.1109/TMTT.1986.1133492.

[5] R. Appleby et al., "Compact real-time (video rate) passive millimeter-wave imager," *Proc. SPIE*, vol. 3703, pp. 13–19, 1999, doi: 10.1117/12.353003.

[6] E. D. Cohen, "The MIMIC program—A retrospective," *IEEE Microw. Mag.*, vol. 13, no. 4, pp. 77–88, May 2012, doi: 10.1109/MMM.2012.2189989.

[7] G. S. Dow et al., "W-band MMIC direct detection receiver for passive imaging system," in *Proc. IEEE MTT-S Int. Microw. Symp. Dig.*, 1993, pp. 163–166, doi: 10.1109/MWSYM.1993.276919.

[8] C. Chen, S. Shi, and D. W. Prather, "Electromagnetic design of an all-diffractive millimeter-wave imaging system," *Appl. Opt.*, vol. 43, no. 12, pp. 2431–2438, Apr. 2004, doi: 10.1364/AO.43.002431.

[9] C. Chen, D. W. Prather, and P. H. Siegel, "Design of a 600 GHz Fresnel lens antenna for passive and active imaging," in *Proc. IEEE Antennas Propag. Soc. Int. Symp.*, 2007, pp. 4385–4388, doi: 10.1109/APS.2007.4396514.

[10] G. R. Huguenin, "Millimeter wave focal plane array imager," *Proc. SPIE*, vol. 2211, pp. 300–301, 1994, doi: 10.1117/12.183005.

[11] R. Olsen, J. A. Lovberg, R. - C. Chou, C. A. Martin, and J. A. Galliano Jr, "Passive millimeter-wave imaging using a sparse phased-array antenna," *Proc. SPIE*, vol. 3064, pp. 63–70, 1997, doi: 10.1117/12.277092.

[12] R. T. Kuroda et al., "Direct-detection MMIC FPAs for MMW imaging," *Proc. SPIE*, vol. 3064, pp. 90–97, Jun. 1997, doi: 10.1117/12.277070.

[13] R. T. Kuroda et al., "Large-scale W-band focal plane array developments for passive millimeter-wave imaging," *Proc. SPIE*, vol. 3378, pp. 57–62, 1998, doi: 10.1117/12.319405.

[14] L. Yujiri et al., "Passive millimeter-wave video camera," *Proc. SPIE*, vol. 3378, pp. 14–19, 1998, doi: 10.1117/12.319397.

[15] L. Yujiri, M. Shoucri, and P. Moffa, "Passive millimeter wave imaging," *IEEE Microw. Mag.*, vol. 4, no. 3, pp. 39–50, Sep. 2003, doi: 10.1109/MMW.2003.1237476.

[16] R. Appleby, D. A. Robertson, and D. Wikner, "Millimeter wave imaging: A historical review," *Proc. SPIE*, vol. 10189, May 2017, Art. no. 1018902, doi: 10.1117/12.2262476.

[17] D. L. McMakin, D. M. Sheen, H. D. Collins, T. E. Hall, and R. R. Smith, "Millimeter-wave high-resolution holographic surveillance system," *Proc. SPIE*, vol. 2092, pp. 525–535, 1994, doi: 10.1117/12.171270.

[18] D. L. McMakin, D. M. Sheen, and T. E. Hall, "Millimeter-wave imaging for concealed weapon detection," *Proc. SPIE*, vol. 5048, pp. 52–62, 2003, doi: 10.1117/12.484704.

[19] J. N. Schulman et al., "W-band direct detection circuit performance with Sb-heterostructure diodes," *IEEE Microw. Wireless Compon. Lett.*, vol. 14, no. 7, pp. 316–318, Jul. 2004, doi: 10.1109/LMWC.2004.829259.

[20] H. P. Moyer et al., "Low noise Sb-heterostructure diode detectors for W-band imaging arrays without RF amplification," *Proc. SPIE*, vol. 5789, pp. 84–92, 2005, doi: 10.1117/12.606730.

[21] H. P. Moyer et al., "Sb-heterostructure diode detector W-band NEP and NEDT optimization," *Proc. SPIE*, vol. 6211, pp. 128–134, 2006, doi: 10.1117/12.667284.

[22] M. R. Abdel-Rahman, F. J. González, and G. D. Boreman, "Antenna-coupled metal-oxide-metal diodes for dual-band detection at 92.5 GHz and 28 THz," *Electron. Lett.*, vol. 40, no. 2, pp. 116–118, Jan. 2004.

[23] A. R. M. Luukanen and V. - P. Viitanen, "Terahertz imaging system based on antenna-coupled microbolometers," *Proc. SPIE*, vol. 3378, pp. 34–44, 1998, doi: 10.1117/12.319403.

[24] F. J. González, M. A. Gritz, C. Fumeaux, and G. D. Boreman, "Two dimensional array of antenna-coupled microbolometers," *Int. J. Infrared Millimeter Waves*, vol. 23, no. 5, pp. 785–797, May 2002, doi: 10.1023/A:1015722821951.

[25] F. J. González, M. Abdel-Rahman, and G. D. Boreman, "Antenna-coupled VOx thin-film microbolometer array," *Microw. Opt. Technol. Lett.*, vol. 38, no. 3, pp. 235–237, 2003, doi: 10.1002/mop.11024.

[26] N. H. Farhat and W. R. Guard, "Millimeter wave holographic imaging of concealed weapons," *Proc. IEEE*, vol. 59, no. 9, pp. 1383–1384, Sep. 1971, doi: 10.1109/PROC.1971.8441.

[27] J. F. Federici et al., "THz imaging and sensing for security applications—Explosives, weapons and drugs," *Semicond. Sci. Technol.*, vol. 20, no. 7, Jun. 2005, Art. no. S266, doi: 10.1088/0268-1242/20/7/018.

[28] M. C. Kemp, "Millimetre wave and terahertz technology for the detection of concealed threats: A review," *Proc. SPIE*, vol. 6402, pp. 90–108, 2006, doi: 10.1117/12.692612.

[29] R. Appleby and R. N. Anderton, "Millimeter-wave and submillimeter-wave imaging for security and surveillance," *Proc. IEEE*, vol. 95, no. 8, pp. 1683–1690, Aug. 2007, doi: 10.1109/JPROC.2007.898832.

[30] T. E. Dillon et al., "Passive, real-time millimeter wave imaging for degraded visual environment mitigation," *Proc. SPIE*, vol. 9471, pp. 10–18, 2015, doi: 10.1117/12.2177356.

[31] A. - I. Sasaki and T. Nagatsuma, "Millimeter-wave imaging using photonic technologies," *NTT Reviewe*, vol. 51, pp. 493–501, Nov. 2002.

[32] P. M. Blanchard, A. H. Greenaway, A. R. Harvey, and K. Webster, "Coherent optical beam forming with passive millimeter-wave arrays," *J. Lightw. Technol.*, vol. 17, no. 3, pp. 418–425, Mar. 1999, doi: 10.1109/50.749381.

[33] A. H. Lettington, D. Dunn, M. Attia, and I. M. Blankson, "Passive millimetre-wave imaging architectures," *J. Opt. A: Pure Appl. Opt.*, vol. 5, no. 4, Jun. 2003, Art. no. S103, doi: 10.1088/1464-4258/5/4/363.

[34] R. D. Martin, C. A. Schuetz, D. W. Prather, and T. E. Dillon, "Controlling the phase of optical carriers," U.S. Patent US8159737, Apr. 17, 2012.

[35] C. A. Schuetz, J. Murakowski, G. J. Schneider, and D. W. Prather, "Radiometric millimeter-wave detection via optical upconversion and carrier suppression," *IEEE Trans. Microw. Theory Techn.*, vol. 53, no. 5, pp. 1732–1738, May 2005, doi: 10.1109/TMTT.2005.847106.

[36] C. A. Schuetz and D. W. Prather, "Optical upconversion techniques for high-sensitivity millimetre-wave detection," *Proc. SPIE*, vol. 5619, pp. 166–174, 2004, doi: 10.1117/12.578961.

[37] C. A. Schuetz, G. J. Schneider, J. Murakowski, and D. W. Prather, "Noise limitations in millimeter wave detection via optical upconversion," *Proc. SPIE*, vol. 5789, pp. 51–58, 2005, doi: 10.1117/12.602378.

[38] C. A. Schuetz et al., "Optical techniques for sparse-aperture millimeter-wave imaging," *Proc. SPIE*, vol. 6211, pp. 96–105, 2006, doi: 10.1117/12.666070.

[39] R. Martin et al., "Design and performance of a distributed aperture millimeter-wave imaging system using optical upconversion," *Proc. SPIE*, vol. 7309, pp. 65–74, 2009, doi: 10.1117/12.818858.

[40] D. W. Prather et al., "Fourier-optics based opto-electronic architectures for simultaneous multi-band, multi-beam, and wideband transmit and receive phased arrays," *IEEE Access*, vol. 11, pp. 18082–18106, 2023, doi: 10.1109/ACCESS.2023.3244063.

[41] K. Maki and C. Otani, "Terahertz beam steering and frequency tuning by using the spatial dispersion of ultrafast laser pulses," *Opt. Exp.*, vol. 16, no. 14, pp. 10158–10169, Jul. 2008, doi: 10.1364/OE.16.010158.

[42] K. Maki, T. Shibuya, C. Otani, K. Suizu, and K. Kawase, "Terahertz beam steering via tilted-phase difference-frequency mixing," *Appl. Phys. Exp.*, vol. 2, no. 2, Feb. 2009, Art. no. 022301, doi: 10.1143/APEX.2.022301.

[43] C. J. Huang, C. A. Schuetz, R. Shireen, S. Shi, and D. W. Prather, "LiNbO$_3$ optical modulator for MMW sensing and imaging," *Proc. SPIE*, vol. 6548, pp. 123–131, 2007, doi: 10.1117/12.718794.

[44] J. Macario et al., "Development of electro-optic phase modulator for 94 GHz imaging system," *J. Lightw. Technol.*, vol. 27, no. 24, pp. 5698–5703, Dec. 2009, doi: 10.1109/JLT.2009.2035641.

[45] J. Macario, C. A. Schuetz, P. Yao, S. Shi, and D. W. Prather, "Development and characterization of LiNbO$_3$ electro-optic phase modulator at 220 GHz for millimeter-wave imaging system," *Proc. SPIE*, vol. 8188, pp. 96–102, 2011, doi: 10.1117/12.898305.

[46] A. J. Mercante et al., "Thin film lithium niobate electro-optic modulator with terahertz operating bandwidth," *Opt. Exp.*, vol. 26, no. 11, pp. 14810–14816, May 2018, doi: 10.1364/OE.26.014810.

[47] J. N. Mait, R. D. Martin, C. A. Schuetz, and D. W. Prather, "Millimeter wave imaging with engineered point spread functions," *Proc. SPIE*, vol. 51, no. 9, May 2012, Art. no. 091606, doi: 10.1117/1.OE.51.9.091606.

[48] J. W. Goodman, *Introduction to Fourier optics*, 4th ed. New York, NY, USA: W.H. Freeman, Macmillan Learning, 2017.

[49] C. A. Schuetz et al., "Sparse aperture millimeter-wave imaging using optical detection and correlation techniques," *Proc. SPIE*, vol. 6548, pp. 74–81, 2007, doi: 10.1117/12.719811.

[50] T. E. Dillon et al., "Passive millimeter wave imaging using a distributed aperture and optical upconversion," *Proc. SPIE*, vol. 7837, pp. 140–147, 2010, doi: 10.1117/12.865081.

[51] C. A. Schuetz, R. D. Martin, T. E. Dillon, and D. W. Prather, "Distributed aperture millimeter-wave imaging," in *Proc. Imag. Appl. Opt.*, 2011, Paper IWB1, doi: 10.1364/ISA.2011.IWB1.

[52] C. Schuetz et al., "Realization of a video-rate distributed aperture millimeter-wave imaging system using optical upconversion," *Proc. SPIE*, vol. 8715, pp. 133–140, 2013, doi: 10.1117/12.2016138.

[53] "ACT-22 selections," NASA Science Mission Directorate, Research Announcement, Nov. 2022. Accessed: Aug. 07, 2023. [Online]. Available: https://nspires.nasaprs.com/external/viewrepositorydocument/cmdocumentid=909340/solicitationId=%7BAA9C7998-5A16-E651-FCE4-1DDAF7BCAB57%7D/viewSolicitationDocument=1/ACT22%20SELECTIONSFINAL.pdf

Dennis W. Prather (Fellow, IEEE) received the BSEE, MSEE, and Ph.D. degree from the University of Maryland, College Park, MD, USA, in 1989, 1993, and 1997, respectively, after serving three years of active duty. He began his professional career by joining the U.S. Navy in 1982 as an E-1, where he served until 2021 and retired at the rank of CAPT (O-6) as an Engineering Duty Officer.

He was a Senior Research Engineer of the Army Research Laboratory, where he performed research on both optical devices and architectures for information processing. In 1997, he joined the Department of Electrical and Computer Engineering, University of Delaware, Newark, DE, USA, where he is currently the College of Engineering Alumni Distinguished Professor. His research interests include theoretical and experimental aspects of RF-photonic elements and their integration into various systems for imaging, communications, and Radar.

Dr. Prather is an Endowed Professor of Electrical Engineering, a Fellow of National Academy of Inventors, Fellow of the Society of Photo-Instrumentation Engineers, and Fellow of the Optica formerly Optical Society of America.

Janusz A. Murakowski received the M.S. degrees in physics from Imperial College, London, U.K., in 1991 and A. Mickiewicz University, Poznan, Poland, in 1990, and the Ph.D. degree in physics from the University of Delaware, Newark, DE, USA, in 1999. He is currently holds the position of a Senior Scientist with Phase Sensitive Innovations, Inc., Newark, DE, USA. He was also an Associate Research Professor with the Department of Electrical and Computer Engineering, University of Delaware, till 2022. He holds 31 issued U.S. patents, an author or coauthor of several books and book chapters, and more than 100 peer-reviewed journal and conference publications. His areas of expertise include electromagnetic science and engineering, micro- and nano-fabrication, and photonic and electro-optic system design and innovation in addition to photonic modeling, design, fabrication, and characterization. His research interests include RF/microwave photonics, including system design, electro-optic modulation, nonlinear optical processes, transmission, detection, and imaging.

Christopher Schuetz received the B.S. degree in electrical engineering from Virginia Polytechnic and State University, Blacksburg, VA, USA, in 1997, and the M.S. and Ph.D. degrees in millimeter-wave imaging from the Graduate School, University of Delaware, Newark, DE, USA, in 2004 and 2007, respectively. Since graduating with honors, he was with companies, such as BAE Systems and Optical Crosslinks, Inc., where his research interests include microwave photonics and polymer optical waveguides. After completing his doctorate, he cofounded Phase Sensitive Innovations, Inc. of Newark, DE, USA, with his advisor Dr. Dennis Prather, where he was a CTO since its founding. He served a dual appointment with the University of Delaware from 2012 to 2015, where he developed techniques for multifunctional receive and transmit phased arrays based on RF photonics. His expertise is in the area of mmW imaging, phenomenology, and detection and RF photonic processing techniques, where he has authored or coauthored more than 100 papers and holds more than 15 patents in this field. In 2015, he returned full time to PSI, but retained an affiliated faculty appointment at UD. He has served on the conference committee for the SPIE Passive Millimeter Wave Imaging Technology Conference. He was the Co-Chair of SPIE Photonics West session on RF and mmW Photonics. He was the Co-Editor of a Special Issue of Applied Optics on RF Imaging.
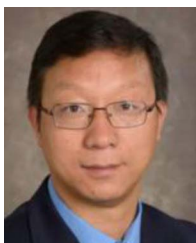
Shouyuan Shi received the B.S., M.S., and Ph.D. degrees in electrical engineering from Xidian University, Xi'an, China, in 1991, 1994, and 1997, respectively. He is currently a Research Professor with the Department of Electrical and Computer Engineering, University of Delaware, Newark, DE, USA. He is also a consulting engineer with Phase Sensitive Innovations, Inc., Newark, DE, USA. He is an author or coauthor of 8 books and book chapters, and more than 380 peer refereed journal and conference publications. He holds more than 20 issued U.S. patents. His research interests include computational electromagnetics, micro-optics and nano-photonics, and RF-photonics technologies and applications, including ultra-wideband RF antennas, optically addressed phase arrays, ultra-wideband electro-optic devices and systems, passive and active millimeter wave imaging systems. He is also an active Reviewer of more than 20 international peer-reviewed journals in the research areas of optics and photonics, RF, electro-optics, and electromagnetics. He was also the Topic Editor of Photonic Devices and Materials, Optical and Photonic Letters, and the Editorial Board Member of Advanced Optics.

Garrett J. Schneider received the B.S. degree in astronomy and physics from Haverford College, Haverford, PA, USA, in 1993, and the Ph.D. degree in physics from the University of Delaware, Newark, DE, USA, in 2002. Since 2002, he has been with the Department of Electrical and Computer Engineering, University of Delaware, where he is currently an Assistant Research Professor. He is also a consulting engineer with Phase Sensitive Innovations, Inc., Newark, DE, USA. He is the coauthor of more than 100 peer-reviewed journals and conference publications, and several books/book chapters, and has 12 issued patents in the fields of nanofabrication and RF photonic system design. His areas of expertise include nonlinear optics, microwave photonics, optical and RF device and system characterization techniques, and nanofabrication. His research interests include RF/microwave/millimeter-wave photonics for applications in telecommunications and remote sensing.

Charles Harrity received the bachelor's degree in physics from the University of Delaware, Newark, DE, USA, in 2009. During this time, he conducted research on Terahertz spectroscopy. He is currently with Phase Sensitive Innovations, Inc., Newark, DE, USA. During his time at PSI, he has researched and developed mmW imaging systems to improve system performance and manufacturability and has been named principal investigator on several projects. He is currently holding the position of Technical Team Lead. He is a co-author on over two dozen peer-reviewed journals and conference publications. His areas of expertise include optical device packaging, mmW imaging, and mmW sensor manufacturing and design.

Zion D. Aranda was born in Newark, DE, USA in 1994. He received the bachelor's degree in electrical engineering from the University of Delaware, Newark, DE, USA, in 2017. During his undergrad, he conducted research for Dr. Dennis Prather on homogeneous integration of organic electro-optic modulators with RF substrates and the fabrication of Fabry-Perot optical cavities for wavelength selective filtering. He joined Phase Sensitive Innovations, Inc. in Newark, DE, USA, shortly after graduating, and led the development of a mmW sensor system to assist helicopter pilots in DVE and hazard avoidance. He is currently a Senior RF Engineer, assisting in several technical efforts surrounding simulation, design, packaging and testing of RF electro-optic packages. His technical skillset include PCB design, analog circuit design, and RF signal testing. His research interests include RF and Optical circuit design, test, and measurement.

Dominic Marinucci was born in Ventnor City, NJ, USA. He received the B.S. degree in physics from Rowan University, Glassboro, NJ, USA, in 2020, and a concentration in photonics. While at Rowan, he researched reverse-micelle interactions using fluorescence correlation spectroscopy under Dr. Nathaniel Nucci. In 2020, he joined Phase Sensitive Innovations, Inc., as an Optical Design Engineer, specializing in free-space optical systems used for phase-sampling and Fourier Imaging. He is currently holding the position of Technical Team Lead for the Optical Processor Team, overseeing the designing, building, and testing of near-infrared optical systems.

Amjed Hallak received the B.S. degree in electrical engineering with a computer science minor from the University of Delaware, Newark, DE, USA, in 2019.

He is currently the Technical Team Leader of Embedded Electronics Systems design, integration, and testing at Phase Sensitive Innovations, Inc., Newark, DE, USA. He has previously maintained leadership in a modernization effort targeted to the University of Delaware's introductory digital design and FPGA course. His expertise resides in SoC Integration, hardware, firmware, and software development. He has optimized and integrated various electronic control systems for systems requiring high data rates and low latency processing for novel RF photonic applications, primarily passive millimeter wave imaging systems.

He has one patent pending corresponding to his work with scalable FPGA integration in RF photonic systems. He became a Member of IEEE Eta Kappa Nu in 2018.

Mathew Zablocki received the B.S. degree in physics from West Chester University, West Chester, PA, USA, in 2007, and the Ph.D. degree in electrical engineering with the University of Delaware, Newark, DE, USA, in 2012. His main research interests include development of silicon-based optical interconnects, and the transfer of photonic devices in thin films. He is Director of photonic applications with Phase Sensitive Innovations, Inc., Newark, DE, USA. He has four patents for photonic devices and is a co-author on more than 20 publications. He has been the Principal Investigator on two SBIR Phase II efforts and contributed to several SBIR/STTR efforts. His current work is focused on increasing performance and the manufacturing readiness level of next-generation lithium niobate modulators.

Matthew Gallion received the B.S. degree in electrical engineering from the University of Delaware, Newark, DE, USA, in 2017. During his undergraduate career with the University of Delaware, he was with a Research Group studying radar and beamforming communication systems. He is currently a Lead R&D Electrical Engineer with Phase Sensitive Innovations (PSI), Inc., Newark, DE, USA. His research interests include power distribution and digital control of devices from system-level to chip-scale integration, and he has a patent pending focusing on scalable, modular phase control of optical channels. He is an IPC Certified Interconnect Designer and leads his team of engineers at PSI in advanced PCB design and power system integration.

Samhit Dontamsetti received the B.S. degree in mechanical engineering with a concentration in aerospace engineering from University of Delaware, Newark, DE, USA, in 2019. During his undergraduate studies, he designed fixtures for glass-fiber-fragmentation testing for ballistics applications with the Center for Composite Materials, Newark, DE, USA. He was also a part of the University of Delaware's Formula Society of Automotive Engineers and Aerospace Society of Automotive Engineers. In 2020, he joined Phase Sensitive Innovations, Inc., Newark, DE, USA, as an Entry Level Mechanical Engineer. He is currently the Technical Team Lead of the Mechanical Engineering, where he oversees the mechanical design and development of mmW imaging systems.

Brian J. Goodman received the National Machinist Journeyman's paper in 1994 through the state of Pennsylvania while working for Hewlett Packard/Agilent Technologies Avondale Division. He came to Phase Sensitive Innovations, Inc. from Northrop Grumman in Elkton, MD, and is currently a Master Senior Machinist. He has an extensive background in medical devices and analytical products and missile defense and space systems.

Jesse Semmel received the B.S. degree in electrical engineering with minors in mathematics and physics from the University of Delaware, Newark, DE, USA, in 2017. During this time, he conducted research on doppler-shift radar technology. In 2017, he joined Phase Sensitive Innovations, Inc. in Newark, DE, USA, as a Photonics Integration Engineer, specializing in modulator and photodiode production and mmW sensor manufacturing and design. Since 2020, he has been overseen the production and design of two passive millimeter-wave imaging systems. He is currently a Project Manager of several projects at PSI.

Robert Lawrence received the B.S. degree in geology from the University of Delaware, Newark, DE, USA, in 1992, and the M.S. degree in telecommunications management from the University of Maryland, College Park, MD, USA, in 2005. He was with the United States Air Force around the world and on multiple deployments as Operations Management, Communications, and then Cyber Officer from 1993 to 2019 and retired as a Joint Qualified Officer at the rank of Lieutenant Colonel (O-5). In 2020, he joined Phase Sensitive Innovations, Inc., where he is currently the Chief Management Officer overseeing more than 20 highly technical R&D and prototyping projects.